Materials Horizons

ROYAL SOCIETY OF CHEMISTRY

COMMUNICATION

View Article Online
View Journal

Cite this: DOI: 10.1039/d5mh01090j

Received 8th June 2025,
Accepted 28th July 2025

DOI: 10.1039/d5mh01090j

rsc.li/materials-horizons

Spectrally-coded optical film for independent transmission and reflection on curved surface

Ji-Eun Yeo, †[a] Hyo Eun Jeong, †[a] Joo Hwan Ko,[ab] Hyeon-Ho Jeong *[acd] and Young Min Song *[e]

Emerging demands for anti-counterfeit security and adaptive camouflage necessitate optical films that conform to the curved transparent substrates of windows, visors, and protective eyewear. These surface-conformal films must deliver high chromatic performance while accommodating geometrical flexibility. Crucially, applications such as hidden displays and directional visual cues require distinct color outputs depending on viewing direction or polarization state. To meet this need, we present a flexible, surface-conformal dual-mode spectral-coded color film (DS-CF) that enables independent control over transmitted and reflected colors. By integrating two resonators within a multilayer thin-film structure, the DS-CF leverages both Lorentzian and Fano-type resonances to realize programmable bi-directional coloration. This design overcomes the limitations of conventional dyes and photonic structures that inherently couple transmission and reflection responses. A painting-inspired demonstration validates the vivid and high-purity color expression in both transmission (≈75%) and reflection (≈41%). Additionally, polarization-sensitive reflectance control is achieved by tailoring the deposition angle of the lossy layer. With scalable fabrication and mechanical flexibility, the DS-CF offers a versatile platform for multifunctional optical films in anti-counterfeit labeling, hidden displays, and adaptive camouflage technologies.

New concepts

In this study, we introduce a flexible dual-mode spectral-coded color film (DS-CF) that enables independent and high-purity control of transmitted and reflected colors through a simple multilayer thin-film architecture. Unlike conventional approaches that rely on complex nanostructures or single-resonator systems with intrinsically coupled spectral responses, our design employs a coupled narrowband and broadband resonator strategy to overcome this spectral interdependence. This enables programmable bi-directional coloration with enhanced chromatic purity, experimentally validated through a painting-inspired demonstration. Additionally, by precisely controlling the deposition angle of the lossy layer, we demonstrate polarization-dependent reflectance modulation, introducing a new dimension of spectral controllability in flexible photonic films. Distinct from existing research, the DS-CF is fully scalable and surface-conformal, as demonstrated by its application on curved substrates in a dual-mode camouflage sheet with angle-dependent hidden display functionality. This work offers new insights to materials science by establishing a versatile platform for multifunctional optical films that integrate structural coloration, polarization control, and surface-conformability, enabling advanced applications in automotive components, wearable optics, and anti-counterfeit visual systems.

1. Introduction

Flexible optical films that can be integrated onto transparent substrates such as windows or protective eyewear offer both aesthetic and functional advantages, including camouflage, hidden displays, and visual encoding for information security. However, conventional color generation methods based on dyes or pigments are inherently limited by a trade-off between optical transmittance and chromatic saturation, often requiring compromises in color vividness to achieve high transparency.[1,2] To overcome this limitation, structural coloration—based on physical nanostructures rather than chemical pigments—has emerged as a promising alternative. Structural colors arise from optical phenomena such as interference, diffraction, and scattering, which are governed by nanoscale geometry rather than molecular absorption, enabling the realization of highly saturated colors. Importantly, structural colors provide significant design

[a] School of Electrical Engineering and Computer Science, Gwangju Institute of Science and Technology, Gwangju 61005, Republic of Korea. E-mail: jeong323@gist.ac.kr
[b] Department of Mechanical Engineering, Massachusetts Institute of Technology, Cambridge, Massachusetts 02139, USA
[c] Department of Semiconductor Engineering, Gwangju Institute of Science and Technology, Gwangju 61005, Republic of Korea
[d] GIST InnoCORE AI-Nano Convergence Initiative for Early Detection of Neurodegenerative Diseases, Gwangju Institute of Science and Technology, Gwangju 61005, Republic of Korea
[e] School of Electrical Engineering, Korea Advanced Institute of Science and Technology, Daejeon 34141, Republic of Korea. E-mail: ymsong@kaist.ac.kr
† These authors contributed equally to this work.

flexibility, as the perceived hue can be finely tuned by adjusting structural parameters such as thickness, periodicity, and refractive index distribution at the nanometer scale.[3–7,57] This level of control surpasses that of conventional pigment-based systems, allowing for more precise color engineering. Furthermore, structurally colored devices exhibit superior environmental durability, resisting UV-induced fading and chemical degradation, thus enabling sustainable and long-lasting designs. These advantages make structural color ideal for security applications such as anti-counterfeit system, where encoded optical features can be hidden within complex background colors. In practice, structural color technologies have been demonstrated in a variety of forms, including 3D chiral structures for full-color printing,[8–10] plasmonic recording media,[11] and hidden image displays based on plasmonic resonances,[12,13] highlighting their versatility and functional potential. More recently, structurally encoded information storage and bioinspired encryption functionalities have been further advanced through approaches such as ice-templated hydrogel architectures and fluorescence-quenching photonic platforms.[58,59]

A representative resonant structure, the metal–insulator–metal (MIM) configuration, enables the generation of highly saturated colors through strong symmetric resonances. However, it inherently couples transmission and reflection spectra, making independent spectral tuning challenging. Meanwhile, structures based on ultrathin resonant layers (UTRLs) require broad absorption to achieve high color purity, necessitating a trade-off with transmittance due to structural constraints.[14] To overcome these limitations and enhance the freedom of color modulation, precise control over mode interactions within the resonant structure is essential. Optical materials are typically characterized by their absorption, transmission, and reflection spectra, which are governed by resonance phenomena occurring at specific wavelengths. These resonance spectra can be broadly categorized based on their line shapes; symmetric Lorentzian profiles, arising from linear interactions between photons and oscillators, and asymmetric Fano profiles, originating from the interference between discrete states and a continuum.[15–20] Among these, Fano resonances have recently garnered significant attention in the field of photonics.[21–24] Traditionally, the implementation of such resonances has relied on precisely engineered nanostructures in meta-surfaces, which offer high design flexibility.[25–41] However, they suffer from scalability limitations due to their subwavelength feature sizes. To overcome these challenges, thin-film-based photonic structures have recently been introduced for Fano resonator design, enabling simplified fabrication processes and cost-effective realization, thereby facilitating practical applications.

In this work, we propose a flexible thin-film resonator capable of simultaneously achieving vivid coloration and partial transparency through a simple multilayer thin-film structure, without relying on complex nanostructures. By coupling two resonators with distinct spectral characteristics—a narrowband resonator and a broadband resonator—the system enables independent control over the transmitted and reflected colors. A color demonstration inspired by a painting experimentally validated the independent control of transmittance and reflectance spectra enabled by the dual-resonator strategy, which overcomes the intrinsic spectral interdependence of conventional single-resonator systems and facilitates bi-directional coloration with enhanced chromatic purity in both transmitted ($\approx$75%) and reflected ($\approx$41%) color. As a practical application, a dual-mode camouflage sheet compatible with curved surfaces was proposed, and polarization-dependent reflectance modulation was demonstrated by precisely engineering the deposition angle of the lossy layer. These findings highlight the potential of the dual-mode spectral-coded color film (DS-CF) platform for advanced optical applications, including hidden pattern displays and polarization-based anti-counterfeit visual cues enabled by angle-dependent color modulation.

2. Results and discussion

2.1 Dual-mode spectral-coded color film.

Fig. 1(A) presents the overall schematic of the DS-CF. This film enables outward visibility through uniformly modulated transmitted colors on the inner surface, while simultaneously exhibiting distinct reflected colors on the outer surface, thereby producing a directionally unique visual effect. The DS-CF comprises two vertically stacked resonators. The lower resonator governs the resonant wavelength of the transmission spectrum, while the inclusion of a secondary resonator in the upper layer provides additional degrees of freedom for tailoring the line shape of the reflection spectrum. Notably, the top layer of the upper resonator incorporates a lossy medium with polarization-sensitive anisotropy, inducing polarization-dependent reflection behavior. In contrast, the transmitted color remains invariant across polarization angle as depicted in Fig. 1(B). This multilayer configuration facilitates independent adjustment of both transmitted and reflected spectra, thereby broadening the applicability of the platform in advanced optical systems requiring dual-mode spectral control. Fig. 1(C) schematically represents the system using a coupled oscillator model, where Oscillator 1 (purple circle) and Oscillator 2 (blue circle) correspond to Resonator 1 (R1), consisting of a metal–insulator–metal (MIM) structure, and Resonator 2 (R2), composed of a lossy medium and a metallic reflector, respectively. These oscillators are coupled with a coupling strength (g), and possess individual resonant frequencies (ω_1 and ω_2) and damping rates (γ_1 and γ_2). This mechanical analogy, coupled oscillators, is commonly employed in photonics to describe interactions between distinct optical resonances.

A strategy is proposed to overcome the intrinsic spectral interdependence between transmittance and reflectance observed in conventional MIM structures, enabling independent optimization of each optical response. Specifically, two principal parameters are modulated: (i) the transmission resonance frequency (ω_1), which determines the transmitted color, and (ii) the reflection spectral profile, which is engineered by controlling the reflection resonance frequency (ω_2) through modulation of the lossy layer thickness in R2. As shown in Fig. 1(D), R1 exhibits

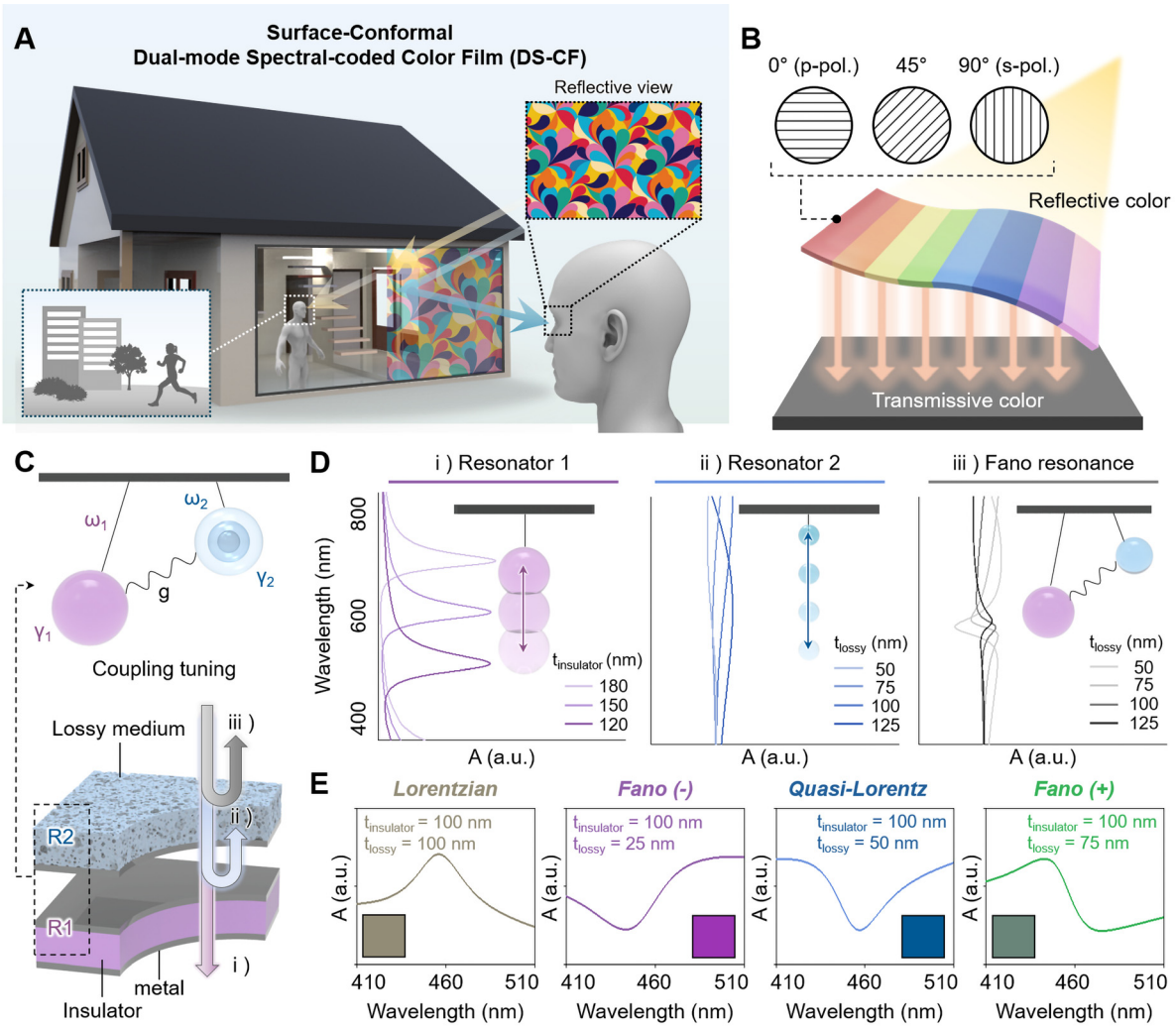

Fig. 1 (A) Schematic of the surface-conformal dual-mode spectral-coded color film (DS-CF). The structure enables outward visibility *via* consistent inner-side transmission, while encoding visual cues through spectrally varied outer-side reflection. (B) Polarization-dependent reflectance of the flexible DS-CF, while preserving polarization-invariant transmission. (C) Weakly coupled oscillator model (top) representing the interaction between the Fabry–Perot cavity (R1) and the ultrathin resonator (R2) in the multilayer thin-film Fano system (bottom). (D) Absorption spectrum profile (right) resulting from the coupling between R1 (left) and R2 (middle), along with the corresponding schematic model. By modulating the individual absorptions of R1 and R2, the combined spectral response can be actively modified. (E) Comparison of absorption spectra for different resonance condition within the 410–510 nm wavelength range and corresponding reflected color.

narrowband resonant peaks centered at 500, 600, and 700 nm when the insulator thickness ($t_{insulator}$) is varied from 120 to 180 nm. In contrast, R2 exhibits broadband absorption characteristics, which are leveraged to modulate ω_2 by incorporating lossy media of varying thickness (t_{lossy} = 50, 75, 100, 125 nm) (Fig. S1). By integrating R1 and R2, each exhibiting distinct optical characteristics, full control of the spectral shape (iii) is realized. This resonant coupling between the two cavities enabled the DS-CF structure to produce a wide range of reflection spectra, thereby facilitating independent modulation of both transmitted and reflected colors *via* dual-mode spectral encoding. Fig. 1(E) visualizes the resulting absorption spectra from the coupling of R1–R2 configuration, demonstrating tunable line shapes ranging from symmetric Lorentzian to asymmetric Fano-like and quasi-Lorentzian profiles. The corresponding reflected colors, shown in the inset, highlight the strong correlation between engineered spectral shape and perceived color.

2.2 Optical calculation of DS-CF

The cross-sectional schematic representation of DS-CF is depicted in Fig. 2(A). This device integrates two optically distinct resonators: a narrowband absorption Fabry–Perot (F–P) cavity (R1), composed of two highly reflective mirrors, and a broadband absorption lossy cavity (R2), consisting of a single mirror, where the refractive index contrast allows it to function effectively as a secondary reflector. Ag was employed as the reflective material in R1 due to its superior reflectivity and high color purity compared to other metals (Fig. S2). In R2, the lossy medium was engineered by tuning the porosity (P_r) of the highly absorbent material. To select the lossy medium, we

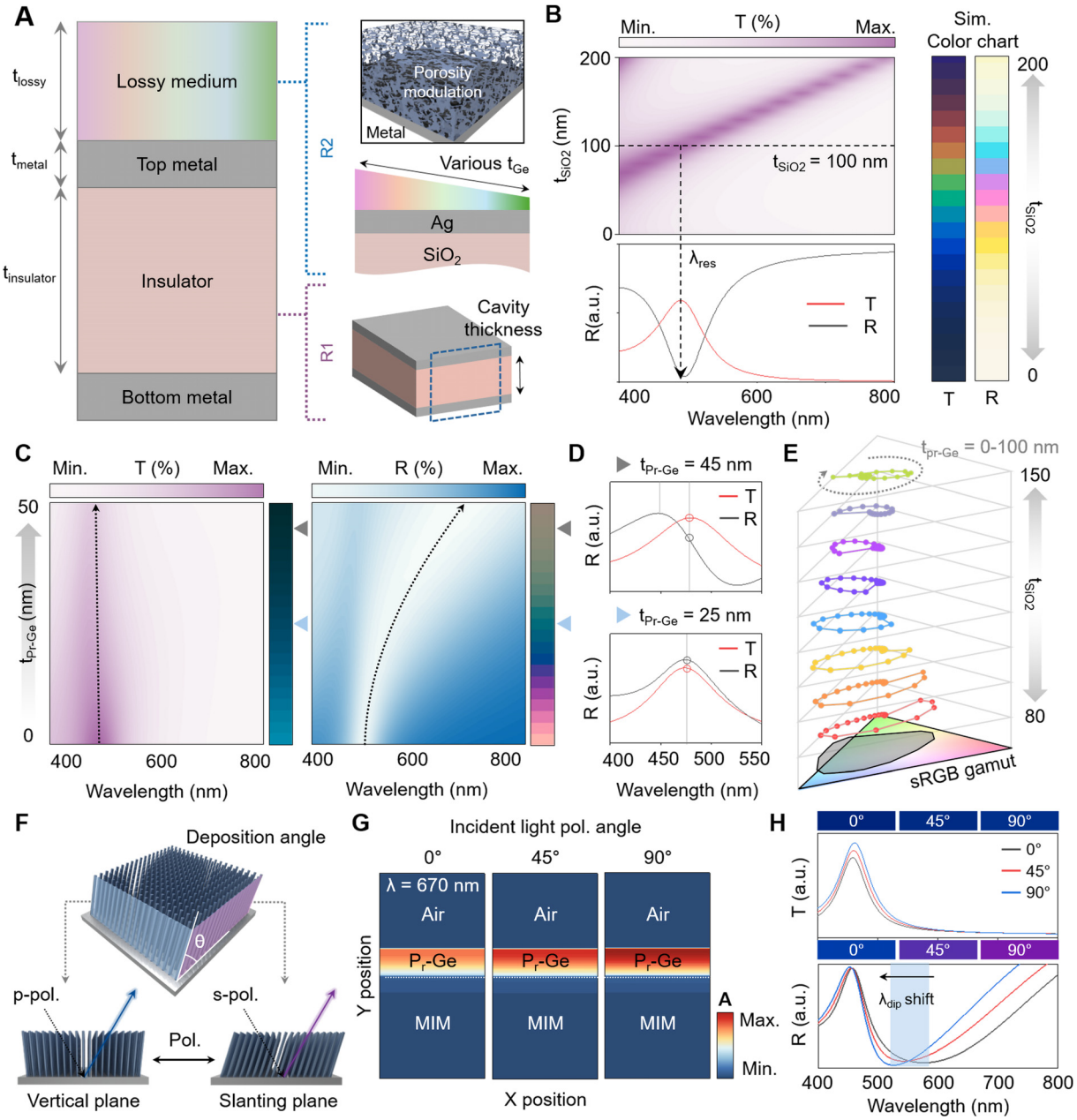

Fig. 2 (A) Schematic of the DS-CF computational model comprising resonators R1 and R2. (B) Contour maps of simulated transmittance spectra (left, top) and corresponding color maps (right) as a function of insulator layer thickness (t_{SiO_2}) in R1. Transmittance and reflectance spectra (left, bottom) demonstrate a complementary color relationship (at t_{SiO_2} = 100 nm). (C) Transmittance and reflectance contour map and corresponding color charts as a function of the lossy layer thickness (t_{Pr-Ge}) after integrating R1 and R2. (D) Transmission and reflection spectra at two different t_{Pr-Ge}. In the t_{Pr-Ge} = 25 nm (top), transmittance and reflectance spectra are engineered to be identical. In contrast, at t_{Pr-Ge} = 45 nm (bottom), while the transmission spectrum remains unchanged, the reflection spectrum is modified to exhibit a Fano (+) spectral shape. (E) 3D surface plot showing sRGB color gamut coverage based on the reflected color as a function of t_{SiO_2} (0–300 nm) and t_{Pr-Ge} (0–100 nm). (F) Schematic illustration of the color switching mechanism based on directional variations in porosity of lossy medium. The perceived porosity changes with in-plane viewing angle, leading to angle-dependent modulation of the optical response and corresponding color variation. (G) Absorption intensity distributions of DS-CF in each polarization at 670 nm. (H) Simulated transmittance and reflectance spectra under different polarization states of incident light, along with the corresponding colors.

chose six representative lossy materials: a-Ge, a-GST, c-GST, Co, a-Si, and TiN. The a-Ge was selected based on its favorable optical properties and compatibility with the thin-film deposition process. The variation in complex refractive indices for these materials is shown in Fig. S3. The P_r of the Ge layer was controlled *via* the glancing angle deposition (GLAD) method using E-beam evaporation, allowing precise tuning of optical absorption characteristics (details in SI1, Fig. S4 and S5). Moreover, the increased P_r of the film allows for precise color tuning as a function of film thickness. In R1, $t_{insulator}$

significantly influences the transmission color of the resonator. In this case, SiO_2 was selected as the insulating layer, and the resonator produces a continuous transmission peak that progressively red-shifts as t_{SiO_2} increases (t_{SiO_2} = 0–200 nm). This behavior is visualized in the contour map of simulated transmittance spectra and the corresponding color chart. The peak position in the transmittance spectrum (red line) is designated as the resonant wavelength (λ_{res}), at which the corresponding reflection spectrum (black line) exhibits a pronounced dip. This spectral alignment gives rise to a complementary color relationship between transmittance and reflectance, resulting from their intrinsic spectral coupling (Fig. 2(B)).

The spectral interaction between the transmission and reflection of R1 can be engineered by combining it with R2. This coupling enables the independent tuning of each mode spectra. Fig. 2(C) highlights the spectral evolution of both transmittance peaks and reflectance dips—along with their respective contour maps and associated color changes—when a Pr–Ge (P_r 70%) layer of varying thickness is deposited on a R1 with a fixed t_{SiO_2} (t_{SiO_2} = 100 nm), where λ_{res} is located at 490 nm. Under these resonant conditions, R1 produces a blue-colored transmission spectrum and a red-colored reflection spectrum, consistently maintaining a complementary color relationship. However, as shown in Fig. 2(D), when $t_{Pr–Ge}$ is 25 nm, the reflection spectrum (black line) exhibits a peak at the same spectral position as the transmission peak (red line), demonstrating a Lorentzian line shape. Furthermore, increasing the $t_{Pr–Ge}$ to 45 nm results in a reflection spectrum characterized by a peak in the short-wavelength region and a dip in the long-wavelength region relative to λ_{res}, indicative of a Fano (+) resonance profile, and giving rise to a brownish reflection color. The chromaticity diagram in Fig. 2(E) presents the calculated reflectance results corresponding to various combinations of t_{SiO_2} and $t_{Pr–Ge}$, mapped within the standard red, green, and blue (sRGB) regions of the CIE color gamut. Additionally, the topmost layer of the DS-CF, composed of a porous medium, exhibits in-plan anisotropy due to local orientation variations induced by the GLAD deposition angle (θ).[42–45] These differences in plane orientation of the geometric structure result in anisotropic responsiveness, inducing structural color changes based on the polarization angle (Fig. 2(F)).[46,47] In our simulations, the polarization-dependent porosity of the lossy material was modeled by incorporating anisotropic optical properties resulting from the GLAD process. Significant differences in both the complex refractive index and reflection spectrum with respect to polarization were observed at a deposition angle of 70°. Accordingly, P_r 70% for p-polarized light, 80% for s-polarized, and 75% for unpolarized light were applied in the model (Fig. S6). Fig. 2(G) shows the simulated absorption profiles as a function of the polarization angle of the incident light at a fixed wavelength of λ = 670 nm. As the polarization angle varies from 0° to 90°, a gradual increase in absorption is observed, indicating that polarization-dependent anisotropy in the lossy layer enables dynamic color modulation. This effect is attributed to orientation-dependent differences in the nanostructured film morphology induced by the deposition angle. The largest color difference (ΔE) in the reflection spectrum was observed under resonant conditions with t_{SiO_2} = 100 nm and $t_{Pr–Ge}$ = 20 nm, while the transmission color remained stable in the blue region. The reflection color, however, shifted from blue to violet with changing polarization angle, as shown in Fig. 2(H). Detailed information on the adjusted layer thickness and ΔE values can be found in Fig. S7. Furthermore, a comparative analysis of ΔE values based on the choice of reflective metal layer revealed that Ag produced the most pronounced polarization-dependent color shift (Fig. S8).

2.3 Painting-inspired DS-CF demonstration and experimental colorimetric analysis

The Fano resonator induces distinct spectral asymmetry, enhancing the optical performance of structural colors by increasing color purity and enabling strong contrast between adjacent regions.[48] This structural color, characterized by a broad color gamut and high chromatic purity, is applicable to various fields such as color printing,[49] spectral encoding,[50] and secure information encryption.[51,52] The reflected and transmitted colors of DS-CF are simply determined by the thicknesses of the F–P resonator and the top lossy layer. As discussed in the previous section, the theoretical design of the DS-CF structure shows that the interaction of multiple resonance modes improves the spectral line shape and expands the achievable color diversity. Fig. 3(A) presents a bidirectional multi-chromatic coloration device with high saturation, featuring color distributions inspired by Danse (Henri Matisse), which are achieved through precise modulation of the insulating layer thickness. The dual-sided optical response exhibits high color purity and reveals distinguishable regions. (Fig. 3(B) and (C)). To realize spatial segmentation through structurally encoded color regions, we implemented that each color was fabricated using an F–P structure with a changing cavity thickness. Specifically, four shadow masks were employed during sequential film deposition steps, resulting in F–P resonators with four distinct insulator thicknesses (70, 110, 130, and 150 nm), as illustrated reflective view in Fig. 3(D) (details in Methods). The first to fourth images in Fig. 3(D) represent the reflection colors observed before the deposition of Resonator 2, where the F–P resonance dominates, whereas the fifth image shows the reflection color after the integration of both Resonator 1 and Resonator 2, corresponding to a Fano resonance. We adopted a Fano resonator that enables spectral tailoring by leveraging the phase difference between a broadband absorber and a narrowband resonator composed of SiO_2 and Ag (Fig. S9). By adjusting the thickness of the insulating layer, the MIM resonator produces transmittance peaks and reflectance dips that correspond to RGB colors and its complementary colors. The Fano resonator asymmetrically modulates the reflectance spectrum (Fig. 3(E), right) while maintaining the same resonant wavelength in the transmission spectrum (Fig. 3(E), left). The color patches displayed next to each spectrum represent the perceived colors derived from the corresponding spectral

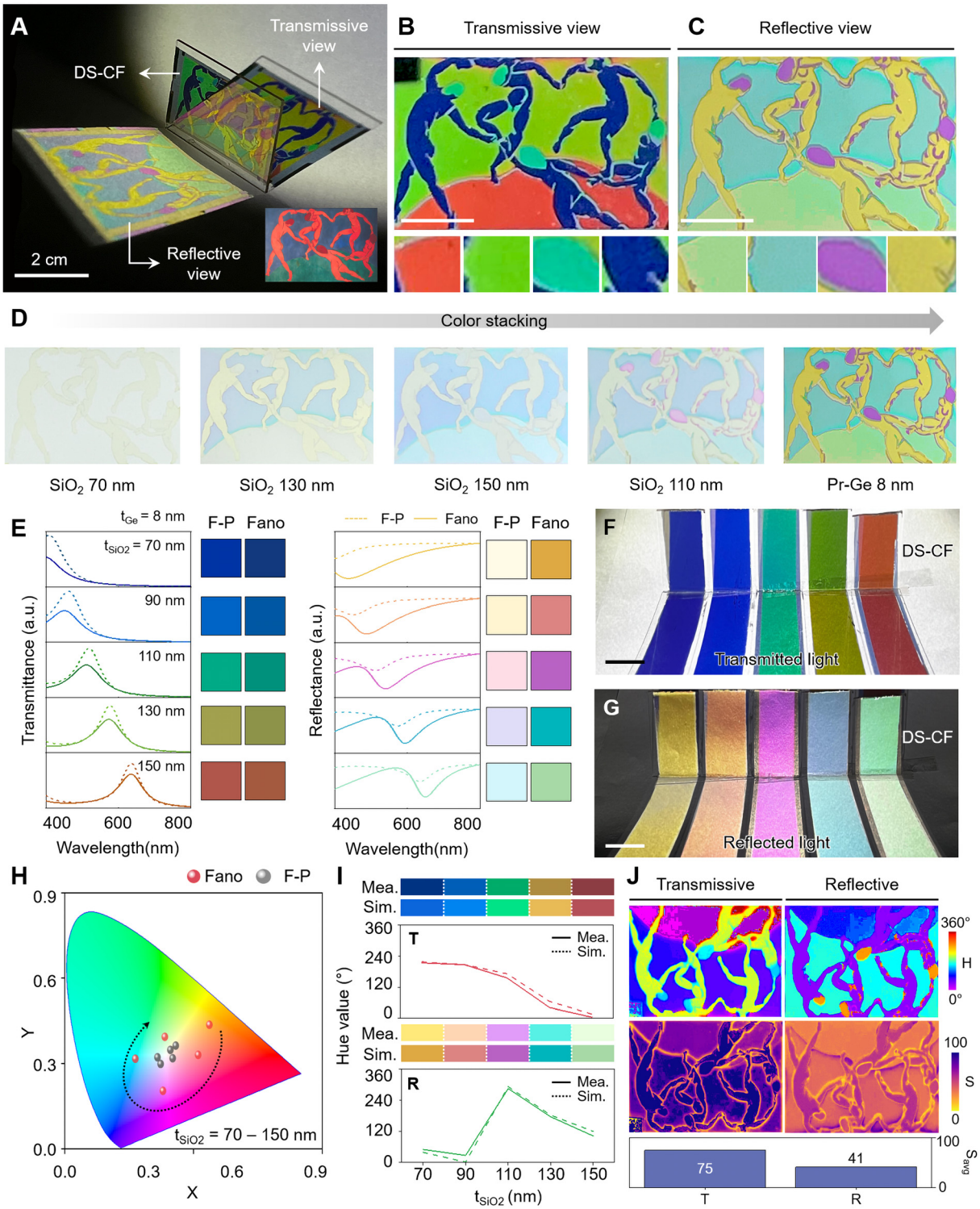

Fig. 3 (A) Photographs of the experimental demonstration of a painting-inspired DS-CF, exhibiting clearly distinguishable color patterns under two viewing directions. The inset shows the original reference image used for the design (''Dance'', created by Henri Matisse, 1869–1954). Measured colors observed from the designated transmission (B) and reflection (C) viewing directions. Each mode presents a distinct set of four colors region. The scale bar is 0.5 cm. (D) Fabrication process for implementing color stacking. To enable distinct color differences in both transmission and reflection mode, t_{SiO_2} was selectively varied (70, 90, 110, 130, and 150 nm), while t_{Pr-Ge} was fixed at 8 nm. (E) simulated transmittance and reflectance spectra under F–P resonator and Fano resonator within the wavelength range from 400–800 nm. (F) and (G) Color image of DS-CF with transmitted light (F) and reflected light (G). The scale bar is 1 cm. (H) CIE 1931 chromaticity diagram with simulated reflected colors under F–P resonator and Fano resonator. (I) Quantitative comparison of experimentally measured and simulated transmission and reflection colors based on extracted Hue values. (J) Hue and saturation analysis of transmitted and reflected colors in the painting-inspired demonstration. Distinct Hue shifts are observed across regions, with the overall sample exhibiting average saturation values above 40, indicative of high color intensity.

profiles, and it can be observed that the F–P and Fano colors in the reflectance spectra closely match the colors shown in Fig. 3(D). The reflectance results are plotted on the CIE diagram, showing that a thin-film resonator with the MIM structure shifts the color coordinates closer to the sRGB gamut. These findings suggest that the proposed F–P structure can be used in optical systems that require resonance selectivity with tunable dual-resonance modes. By enabling selective control over the reflected wavelength, this spectral tuning is well-suited for the realization of bidirectional displays, such as beam-splitting color filter with independently designed transmission and reflection colors. Moreover, enhanced absorption at the target wavelength leads to a narrow reflection dip, thereby improving color purity. Fig. 3(F) and (G) shows that the calculated color closely matches the experimental results. Furthermore, CIE 1931 color gamut demonstrates that the asymmetric spectrum arising from the dual-resonator structure, thereby enhancing the quality of the target color (Fig. 3(H)). To validate the accuracy of the calculation, we compared the hue values with experimental results, confirming strong consistency in Fig. 3(I). On the other hand, in the context of colorful display applications, optical parameters such as contrast with adjacent colors and saturation are key factor for effective visual perception. From this perspective, the DS-CF achieves average saturation levels of approximately 75% in transmission and 41% in reflection, confirming its suitability for display applications (Fig. 3(J)). Finally, these results demonstrate that independent control over both transmission and reflection colors enables a broad color tunability with enhanced chromatic quality.

2.4 Surface-conformal photonic film for camouflage and anti-counterfeit application

To validate the practical applicability of DS-CF, a surface-conformal bi-directional camouflage sheet was fabricated and systematically characterized. A schematic representation of the experimental measurement setup is presented (Fig. 4(A), top). To ensure mechanical flexibility and adaptability with non-planar surfaces, the DS-CF was constructed on a polyvinyl chloride (PVC) substrate. For a demonstration of its camouflage functionality, a DS-CF incorporating a designed camouflage pattern was centrally placed on a background with a matching printed pattern and mounted on a transparent substrate. Under white light illumination, both reflected and transmitted optical responses were evaluated to verify dual-mode spectral modulation (Fig. S10). The fabricated DS-CF incorporated an R1 resonator with a fixed SiO_2 layer thickness (t_{SiO_2}) of 80 nm, deposited on a 2-inch flexible substrate. The progression of the color stacking process and the corresponding thickness profile of the lossy medium are detailed in Fig. S11. The measured transmitted (left) and reflected (right) color images of the DS-CF are shown in Fig. 4(A) (bottom). In reflection, the DS-CF exhibited spectral characteristics closely matching the surrounding printed camouflage, resulting in a visually continuous and indistinguishable appearance between the two regions. In contrast, the transmitted view revealed a distinct blue-toned coloration through the DS-CF area, while the printed camouflage background produced only a shadow on the wall, confirming selective spectral control. Colorimetric analysis of the samples fabricated with different t_{Pr-Ge} confirmed that the DS-CF and the printed camouflage pattern exhibit highly similar optical characteristics in reflection (Fig. S12). As a proof of concept, the DS-CF was implemented as a surface-conformal photonic visor panel, addressing the need for surface-functional films in automotive sunroofs that conform to curved transparent surfaces while providing both aesthetic appeal and controlled light transmission.[53] The fabricated panel was engineered to display visually distinct graphic patterns on the vehicle exterior, thereby demonstrating both functional versatility and aesthetic utility (Fig. 4(B), bottom; Fig. S13).

In addition, the DS-CF-based camouflage sheet can serve as a polarization-dependent visual cue for anti-counterfeiting applications in commercial products.[54] As shown in Fig. 4(C), the DS-CF exhibits distinct optical functionalities at different viewing angles (90° and 45°), demonstrating its potential for dual-mode operation: anti-counterfeit verification and hidden display. This mode separation is enabled by the angular dependence of the DS-CF, which allows different optical responses to be selectively revealed depending on the viewing direction (Fig. S14). To experimentally validate the polarization-dependent optical response, the topmost layer of the DS-CF was patterned into two orthogonally oriented regions. Each region was engineered to exhibit distinct colorimetric shifts under specific polarization states, enabling clear differentiation in color contrast (ΔE) on the incident polarization angle. At a viewing angle of 45°, Fig. 4(D) and (E) illustrate the polarization-dependent switching of encoded optical information by rotating the analyzer angle ((i) hidden display mode). At a polarization angle of 0°, the letter image embedded in Pixel B is indistinct, whereas it becomes clearly discernible under orthogonal polarization, indicating effective polarization-dependent contrast control. Quantitative chromaticity analysis of the sample image reveals that the hue difference between the designated pixel and the background approaches 60°, indicating a high level of visual contrast. The white dashed line denotes the pixel region selected for analysis, where contrast is defined as the difference in hue values (Fig. 4(F)). Under normal incidence with unpolarized light, the DS-CF-based authentic product showed a color appearance nearly identical to that of counterfeit samples (Fig. 4(G), (ii) anti-counterfeit visual cue). However, when viewed through a linear polarizer rotated to a specific angle, only the authentic sample exhibited a noticeable color shift, allowing clear identification. Fig. 4(H) and (I) show the reflected colors of the fabricated samples under different polarization states. Pixel A and Pixel B were designed to respond differently to polarization, enabling clear visual identification (Fig. S15). For example, when the polarization angle is rotated to 90°, Pixel A shows a distinct color change from orange to green, while Pixel B remains nearly unchanged. Fig. 4(J) presents the calculated ΔE values for each pixel, derived from the measured photographic data for both scenarios, represented as a contour map. The cross-sectional profiles along the *x*- and *y*-axes reveal

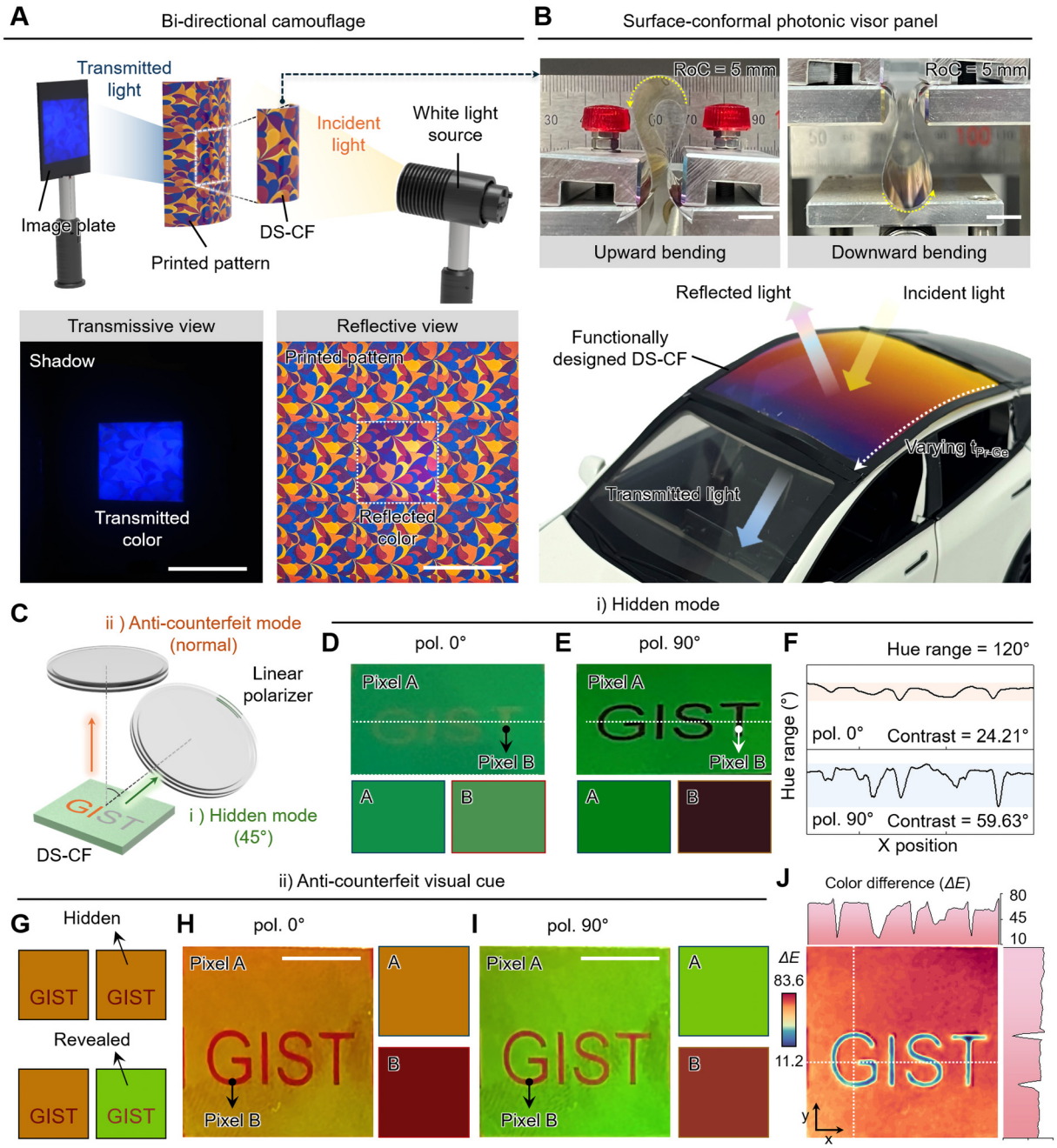

Fig. 4 (A) Schematic of the experimental measure setup (top) for the flexible bi-directional camouflage DS-CF applied to a curved transparent substrate. Photographic images of transmission mode (bottom, left) and reflection mode (bottom, right), aligned with a printed camouflage background to demonstrated dual-mode optical functionality. The scale bar is 5 cm. (B) Photograph of the flexible DS-CF during *in situ* optical measurement under mechanical bending with a bending radius of 5 mm (top). Visual demonstration of the DS-CF based flexible photonic visor panel under mechanical deformation, highlighting practical applicability on curved surfaces (bottom). (C) Schematic of the optical modes modulated by polarized incident light at different angles. At normal incidence (90°), the device operates in anti-counterfeit detection mode, whereas at oblique angle of 45°, it functions as a hidden display mode. Polarization-dependent letter images and corresponding color values at pixel positions A and B under polarizer orientations of 0° (D) and 90° (E). (F) Quantitative analysis of hue contrast as a function of polarizer angle, where hue contrast is defined as the variation in hue values within a fixed hue range of 120°. (G) Schematic of a polarization-based camouflage anti-counterfeit visual cue. Polarization-dependent visual response of the anti-counterfeit cue and the corresponding colors in each region. At a polarization angle of 0°, the hidden visual cue is concealed by the surrounding pattern (H), whereas at 90° (I), the hidden pattern becomes clearly visible. (J) Color difference (ΔE) analysis between two perpendicular polarization states, presented for individual pixels as well as along cross-sectional profiles in the *x*- and *y*-axes. Pixel A exhibits a substantial color difference between the two polarization states, while Pixel B demonstrates minimal color variation.

a substantially higher ΔE in the Pixel A region, while the Pixel B region exhibits minimal color variation. Leveraging the angular-dependent color response of the DS-CF, an additional application concept is proposed, demonstrating its potential as a hidden pattern display.

3. Conclusion

In conclusion, we present a flexible thin-film resonator incorporating a lossy medium, capable of mode-selective spectral line shape tuning. The designed resonator allows selective color tuning by independently controlling transmission and reflection spectra through the manipulation of two coupled resonators, thereby improving the inherent spectral constraints of single-resonator systems. By precisely adjusting the thicknesses of the F–P and UTRL, we effectively controlled the coupling between the two resonant modes which quasi-Lorentzian, Lorentzian, Fano (+), and Fano (−). The dual-resonator configuration enhances both reflective ($\approx$41%) and transmissive color purity ($\approx$75%) by mitigating the spectral constraints, with each region exhibiting excellent agreement with the simulated color designs and demonstrating distinct hue and saturation characteristics. For practical validation, the DS-CF was successfully realized on a flexible substrate as a surface-conformal photonic visor panel, demonstrating vivid, bi-directionally encoded graphics compatible with curved automotive sunroof. Additionally, a dual-mode camouflage sheet was fabricated, enabling seamlessly blending with printed camouflage patterns in reflection while presenting a distinct single transmitted color, thereby validating its capability for advanced display and security applications. Moreover, leveraging polarization-dependent modulation through precise control of the lossy layer orientation, the DS-CF exhibited strong anti-counterfeit visual cues, achieving ΔE values exceeding 80 under varying polarizer angles and enabling hidden pattern displays. These demonstrations underscore the versatility and scalability of the DS-CF platform, positioning it as a promising candidate for integration into multifunctional photonic devices, including dynamic automotive components, wearable optical encryption system, and interactive hidden display technologies.

4. Experimental

4.1. Optical simulation

To analysis optical characteristics, including the spectral shape, phase, and absorption profile from Fano resonator in visible range were calculated by rigorous coupled-wave-analysis (DiffractMod, Rsoft Design Group, USA). The complex refractive index of the lossy material depending on its porosity, was calculated using the volume average theory (VAT) from bulk thin film *via* MATLAB (MathWorks, Inc.) software optical parameters of reference materials such as Au were sourced from previously reported literature.[55,56] A customized MATLAB code was developed to convert simulated and measured reflectance spectra from the Fano resonator into corresponding color information, including color difference (ΔE), hue (H), and saturation (S) values, across the visible wavelength in the range of 400 nm to 800 nm.

4.2. Fabrication of DS-CF

The DS-CF were fabricated *via* a sequential process. Commercial glass substrates or flexible PVC films were selected according to the mechanical requirements of the application. The transparent substrates were *via* ultrasonic treatment cleaned with acetone and IPA, then mounted onto a rigid support. Each layer of the DS-CF was subsequently deposited in high vacuum ($\approx 10^{-6}$ Torr) using electron beam evaporator (KVEE2000, Korea Vacuum Tech Co., South Korea). The lossy material (Ge) was deposited using glancing angle deposition (GLAD) process in a customized sample holder with the thickness controlled by a deposition rate of 1 Å s^{-1}. The painting-inspired sample shown in Fig. 3(A) was manufactured by initially depositing a 25 nm Ag layer. Subsequently, SiO_2 and Ag were selectively deposited onto predefined regions using a shadow mask to construct spatially distinct MIM resonators corresponding to the desired colors. Then, Pr–Ge layer was conformally deposited over the entire substrate surface, completing the fabrication of the colorful patterned sample (details in Fig. S16). Each color region of the flexible camouflage sample was composed of the same MIM structure, consisting of a 25 nm Ag layer and an 80 nm SiO_2 layer (Fig. 4(A)). The thickness of the lossy layer was adjusted by dry etching using a reactive ion etching (RIE) system (PLASMA LAB80, Oxford, USA) with CF_4 gas.

4.3. Spectral measurements

Reflectance and transmittance spectra were obtained at normal incidence by changing the position of the detector. The measurement system consisted of a Xe lamp (SLS400, Thorlabs, USA) and a spectrometer (OCEAN-HDX-VIS-NIR, Ocean Insight, USA), with collimated light delivered through optical fiber. The detector collected the light reflected or transmitted along the normal direction, and the recorded spectra inherently included the optical contributions from the glass substrate. The surface-conformal camouflage sample was arranged between printed reference patterns and mounted onto a transparent plate for alignment in optical measurements. The reflected and transmitted light from the sample was projected onto image plates aligned normally.

Author contributions

Ji-Eun Yeo: writing – original draft, validation, methodology, data curation, conceptualization. Hyo Eun Jeong: writing – original draft, methodology, investigation, formal analysis. resources, methodology. Joo Hwan Ko: formal analysis, conceptualization. Hyeon-Ho Jeong: writing – review & editing, supervision. Young Min Song: writing – review & editing, supervision, project administration, conceptualization.

Conflicts of interest

There are no conflicts to declare.

Data availability

The data supporting this article have been included as part of the SI.

Supplementary information is available. See DOI: https://doi.org/10.1039/d5mh01090j

Acknowledgements

This work was supported by the National Research Foundation of Korea (NRF) grant funded by the Korea government (MSIT) (RS-2025-16902996, RS-2023-NR077254, RS-2021-NR057359). This material was also supported by the Technology Innovation Program (RS-2024-00467230, Development of a Digital Healthcare Device for Non-invasive Continuous Monitoring of Myocardial Infarction Biomarkers Based on Mid-Infrared Nano-Optical Filters) funded by the Ministry of Trade Industry & Energy (MOTIE, Korea). This work was also funded by InnoCORE-GIST program of the Ministry of Science and ICT.

References

1 K.-T. Lee, S. Y. Han, Z. Li, H. W. Baac and H. J. Park, *Sci. Rep.*, 2019, **9**, 14917.
2 R. W. Sabnis, *Displays*, 1999, **20**, 119–129.
3 C. Yang, W. Shen, Y. Zhang, K. Li, X. Fang, X. Zhang and X. Liu, *Sci. Rep.*, 2015, **5**, 9285.
4 C.-S. Park, V. R. Shrestha, S.-S. Lee, E.-S. Kim and D.-Y. Choi, *Sci. Rep.*, 2015, **5**, 8467.
5 C.-S. Park, V. R. Shrestha, S.-S. Lee and D.-Y. Choi, *Sci. Rep.*, 2016, **6**, 25496.
6 K. T. Lee, C. Ji, D. Banerjee and L. J. Guo, *Laser Photonics Rev.*, 2015, **9**, 354–362.
7 C. Yang, W. Shen, J. Zhou, X. Fang, D. Zhao, X. Zhang, C. Ji, B. Fang, Y. Zhang and X. Liu, *Adv. Opt. Mater.*, 2016, **4**, 1981.
8 H. Liu, B. Zhang, T. Gao, X. Wu, F. Cui and W. Xu, *Nanoscale*, 2019, **11**, 5506–5511.
9 W.-J. Chung, J.-W. Oh, K. Kwak, B. Y. Lee, J. Meyer, E. Wang, A. Hexemer and S.-W. Lee, *Nature*, 2011, **478**, 364–368.
10 K. E. Shopsowitz, H. Qi, W. Y. Hamad and M. J. MacLachlan, *Nature*, 2010, **468**, 422–425.
11 E. Heydari, J. R. Sperling, S. L. Neale and A. W. Clark, *Adv. Funct. Mater.*, 2017, **27**, 1701866.
12 D. Franklin, S. Modak, A. Vázquez-Guardado, A. Safaei and D. Chanda, *Light: Sci. Appl.*, 2018, **7**, 93.
13 E. D. Finlayson, I. R. Hooper, C. R. Lawrence, M. Heath, D. Anderson, J. R. Sambles and P. Vukusic, *Adv. Opt. Mater.*, 2018, **6**, 1700843.
14 M. A. Kats, R. Blanchard, P. Genevet and F. Capasso, *Nat. Mater.*, 2013, **12**, 20–24.
15 C. Ott, A. Kaldun, P. Raith, K. Meyer, M. Laux, J. Evers, C. H. Keitel, C. H. Greene and T. Pfeifer, *Science*, 2013, **340**, 716–720.
16 D. M. Riffe, *Phys. Rev. B: Condens. Matter Mater. Phys.*, 2011, **84**, 064308.
17 U. Fano, *Phys. Rev.*, 1961, **124**, 1866.
18 J. M. Blatt and V. F. Weisskopf, *Theoretical nuclear physics*, Springer Science & Business Media, 2012.
19 R. Madden and K. Codling, *Phys. Rev. Lett.*, 1963, **10**, 516.
20 J. A. Fan, C. Wu, K. Bao, J. Bao, R. Bardhan, N. J. Halas, V. N. Manoharan, P. Nordlander, G. Shvets and F. Capasso, *Science*, 2010, **328**, 1135–1138.
21 M. F. Limonov, M. V. Rybin, A. N. Poddubny and Y. S. Kivshar, *Nat. Photonics*, 2017, **11**, 543–554.
22 A. Kaldun, A. Blättermann, V. Stooß, S. Donsa, H. Wei, R. Pazourek, S. Nagele, C. Ott, C.-D. Lin and J. Burgdörfer, *Science*, 2016, **354**, 738–741.
23 M. ElKabbash, T. Letsou, S. A. Jalil, N. Hoffman, J. Zhang, J. Rutledge, A. R. Lininger, C.-H. Fann, M. Hinczewski and G. Strangi, *Nat. Nanotechnol.*, 2021, **16**, 440–446.
24 Z. Wang, Y. L. Ho, T. Cao, T. Yatsui and J. J. Delaunay, *Adv. Funct. Mater.*, 2021, **31**, 2102183.
25 Q. Zhang, X. Wen, G. Li, Q. Ruan, J. Wang and Q. Xiong, *ACS Nano*, 2013, **7**, 11071–11078.
26 F. Hao, P. Nordlander, Y. Sonnefraud, P. V. Dorpe and S. A. Maier, *ACS Nano*, 2009, **3**, 643–652.
27 H.-D. Deng, X.-Y. Chen, Y. Xu and A. E. Miroshnichenko, *Nanoscale*, 2015, **7**, 20405–20413.
28 Y. Zhang, Y.-R. Zhen, O. Neumann, J. K. Day, P. Nordlander and N. J. Halas, *Nat. Commun.*, 2014, **5**, 4424.
29 N. S. King, L. Liu, X. Yang, B. Cerjan, H. O. Everitt, P. Nordlander and N. J. Halas, *ACS Nano*, 2015, **9**, 10628–10636.
30 B. Hopkins, A. N. Poddubny, A. E. Miroshnichenko and Y. S. Kivshar, *Phys. Rev. A: At., Mol., Opt. Phys.*, 2013, **88**, 053819.
31 D. Bekele, Y. Yu, K. Yvind and J. Mork, *Laser Photonics Rev.*, 2019, **13**, 1900054.
32 Y. Xu and A. E. Miroshnichenko, *Phys. Rev. B: Condens. Matter Mater. Phys.*, 2014, **89**, 134306.
33 Y. Liu, X. Weng, M. Wang, W. Li, S. Ma, L. Zhang, P. Zhou and L. Deng, *ACS Photonics*, 2022, **9**, 888–894.
34 Y. Hua, A. K. Fumani and T. W. Odom, *ACS Photonics*, 2019, **6**, 322–326.
35 K.-L. Lee, M.-L. You, X. Shi, Y.-R. Li, K. Ueno, H. Misawa and P.-K. Wei, *Appl. Mater. Today*, 2019, **16**, 72–82.
36 D. L. Sounas and A. Alù, *Phys. Rev. B*, 2018, **97**, 115431.
37 S. H. Wu, K. L. Lee, A. Chiou, X. Cheng and P. K. Wei, *Small*, 2013, **9**, 3532–3540.
38 W. X. Lim, M. Manjappa, Y. K. Srivastava, L. Cong, A. Kumar, K. F. MacDonald and R. Singh, *Adv. Mater.*, 2018, **30**, 1705331.
39 M. Manjappa, Y. K. Srivastava, L. Cong, I. Al-Naib and R. Singh, 2017.
40 N. Liu, T. Weiss, M. Mesch, L. Langguth, U. Eigenthaler, M. Hirscher, C. Sonnichsen and H. Giessen, *Nano Lett.*, 2010, **10**, 1103–1107.
41 N. Papasimakis and N. I. Zheludev, *Opt. Photonics News*, 2009, **20**, 22–27.
42 Y. J. Yoo, J. H. Ko, G. J. Lee, J. Kang, M. S. Kim, S. G. Stanciu, H. H. Jeong, D. H. Kim and Y. M. Song, *Adv. Mater.*, 2022, **34**, 2110003.

43 Y. J. Yoo, J. H. Ko, W.-G. Kim, Y. J. Kim, D.-J. Kong, S. Kim, J.-W. Oh and Y. M. Song, *ACS Appl. Nano Mater.*, 2020, **3**, 6636–6644.
44 Y. J. Yoo, W. G. Kim, J. H. Ko, Y. J. Kim, Y. Lee, S. G. Stanciu, J. M. Lee, S. Kim, J. W. Oh and Y. M. Song, *Adv. Sci.*, 2020, **7**, 2000978.
45 J. E. Yeo, J. H. Ko, S. H. Lee and Y. M. Song, *Adv. Electron. Mater.*, 2025, 2400977.
46 J. H. Ko, Y. J. Yoo, Y. J. Kim, S. S. Lee and Y. M. Song, *Adv. Funct. Mater.*, 2020, **30**, 1908592.
47 J. H. Ko, S.-H. Hong, S.-K. Kim and Y. M. Song, *iScience*, 2023, **26**, 107946.
48 M. ElKabbash, N. Hoffman, A. R. Lininger, S. A. Jalil, T. Letsou, M. Hinczewski, G. Strangi and C. Guo, *Nat. Commun.*, 2023, **14**, 3960.
49 M. Song, L. Feng, P. Huo, M. Liu, C. Huang, F. Yan, Y.-Q. Lu and T. Xu, *Nat. Nanotechnol.*, 2023, **18**, 71–78.
50 P. Zijlstra, J. W. Chon and M. Gu, *Nature*, 2009, **459**, 410–413.
51 J. H. Ko, J.-E. Yeo, H. E. Jeong, D. E. Yoo, D. W. Lee, Y.-W. Oh, S. Jung, I.-S. Kang, H.-H. Jeong and Y. M. Song, *Nanophotonics*, 2024, **13**, 1119–1129.
52 H. Lochbihler, *Adv. Opt. Technol.*, 2015, **4**, 71–77.
53 A. Krasnov, *Opt. Mater.*, 2023, **135**, 113302.
54 J. H. Lee, Y. J. Kim, Y. J. Yoo, S. Chang, G. J. Lee, J. H. Ko, K. M. Kang, D. Chanda and Y. M. Song, *Adv. Opt. Mater.*, 2021, **9**, 2100429.
55 A. Garahan, L. Pilon, J. Yin and I. Saxena, *J. Appl. Phys.*, 2007, **101**, 014320.
56 D. L. Windt, W. C. Cash Jr, M. Scott, P. Arendt, B. Newnam, R. Fisher and A. Swartzlander, *Appl. Opt.*, 1988, **27**, 246–278.
57 H. M. Kim, J. Lee, J. Kim, G. Kim, J.-H. Han, J. H. Ko, Y. M. Song and H.-H. Jeong, *Adv. Mater.*, 2025, 2511261.
58 F. Bian, L. Sun, L. Cai, Y. Wang and Y. Zhao, *Proc. Natl. Acad. Sci. U. S. A.*, 2020, **117**, 22736–22742.
59 S. Miao, Y. Wang, L. Sun and Y. Zhao, *Nat. Commun.*, 2022, **13**, 4044.